The interplay between thermodynamics and kinetics in the solid-state synthesis of layered oxides

Matteo Bianchini[§ a,b,c], Jingyang Wang[§ a,b], Raphaële Clément [b,d], Bin Ouyang [a,b], Penghao Xiao[a,b], Daniil Kitchaev[d], Tan Shi [a,b], Yaqian Zhang [a,b], Yan Wang [e], Haegyeom Kim [a,b], Mingjian Zhang [f], Jianming Bai[f], Feng Wang [f], Wenhao Sun[a,b, *] and Gerbrand Ceder[a,b, *]

§equal contribution

*corresponding authors:
Dr. Wenhao Sun (Email: wenhaosun@lbl.gov)
Prof. Gerbrand Ceder (Email: gceder@berkeley.edu)

[a] Materials Sciences Division, Lawrence Berkeley National Laboratory, Berkeley, CA 94720, USA
[b] Department of Materials Science and Engineering, University of California, Berkeley, CA 94720 USA
[c] Battery and Electrochemistry Laboratory, Institute of Nanotechnology, Karlsruhe Institute of Technology (KIT), Hermann-von-Helmholtz-Platz 1, 76344 Eggenstein-Leopoldshafen, Germany
[d] Materials Department, University of California Santa Barbara, Santa Barbara, CA 93106, USA
[e] Samsung Advanced Institute of Technology - USA, 255 Main Street, Suite 702, Cambridge, Massachusetts 02142, United States
[f] Brookhaven National Laboratory, Upton, NY 11973, USA.

Abstract

In the synthesis of inorganic materials, reactions often yield non-equilibrium kinetic byproducts instead of the thermodynamic equilibrium phase. Understanding the competition between thermodynamics and kinetics is fundamental towards the rational synthesis of target materials. Here, we use *in situ* synchrotron X-ray diffraction to investigate the multistage crystallization pathways of the important two-layer (P2) sodium oxides $Na_{0.67}MO_2$ (M = Co, Mn). We observe a series of fast non-equilibrium phase transformations through metastable three-layer O3, O3' and P3 phases before formation of the equilibrium two-layer P2 polymorph. We present a theoretical framework to rationalize the observed phase progression, demonstrating that even though P2 is the equilibrium phase, compositionally-unconstrained reactions between powder precursors favor the formation of non-equilibrium three-layered intermediates. These insights can guide the choice of precursors and parameters employed in the solid-state synthesis of ceramic materials, and constitutes a step forward in unraveling the complex interplay between thermodynamics and kinetics during materials synthesis.

Introduction

Designing and synthesizing new materials with tailored properties are cumbersome tasks. When approaching materials synthesis, the thermodynamic phase diagram is often a general starting point. Guided by it, one should prepare precursors at a composition where a desired equilibrium phase is stable, and obtain it by holding the system under appropriate thermodynamic conditions (temperature and pressure) for a sufficiently long time. Both experimental and *ab-initio* predicted phase diagrams are guiding tools for synthesis [1, 2, 3], yet they often become unreliable when reaction kinetics plays a major role. Notably, compounds predicted as thermodynamically stable often cannot be synthesized experimentally [4], whereas metastable materials (i.e. higher in energy than the ground state phases) are often observed during materials formation [5, 6].

Several *in situ* studies of synthesis reactions [7, 8, 9, 10, 11, 12, 13, 14, 15] have shown that the path towards the target phase often proceeds through multiple non-equilibrium intermediates. This pathway is important as long-lived metastable intermediates can persist as impurity phases in the final product, or they can structurally template ensuing phase transformations [11, 12, 13]. Although kinetic factors can be exploited to guide the outcome of specific reactions [12, 13], currently no general guiding principles exist to predict or

3

rationalize these pathways, which can be entirely thermodynamic, kinetic, or result from the intricate interplay of the two.

A milestone in building a predictive theory of synthesis is being able to account for and anticipate these metastable intermediates. Understanding the competition between thermodynamics and kinetics is key to the predictability of synthesis reactions. This is especially important given the emergence of computational materials-by-design methods, which have dramatically increased the number of compelling materials to be experimentally investigated [16]. Yet scientists still lack tools to predict the synthetic accessibility of these novel compounds, or the pathways by which a stable or metastable phase will form [5].

In this paper, we systematically investigate the non-equilibrium formation pathways of layered Na metal oxides by means of *in situ* synchrotron X-ray diffraction and *ab-initio* computations. We chose these Na-based compounds due to their technological relevance as battery electrodes [17], thermoelectrics [18] and superconducting materials [19]; as well as for their structural complexity with many competing phases [20, 21, 22, 23]. The layered Na_xMO_2 structures form in two major polytypes, which can be distinguished by their oxygen stacking sequence and Na environments (Figure 1b): P2, with a two-layer stacking; and O3 and P3, with a three-layer stacking. Properties such as Na^+ mobility and electronic and thermal conductivity are highly dependent on the

4

stoichiometry and structure of the Na_xMO_2 phase under consideration. For example, P2 phases are attractive Na-ion cathode materials exhibiting excellent Na^+ conductivity [24, 25].

Understanding practical synthesis routes to these specific Na_xMO_2 structures is essential. The thermodynamic stability of different Na_xMO_2 polytypes varies with the Na content, x, as calculated in Figure 1a. In the Na_xCoO_2 system, the O3/O3'-type stacking (O3/O3' are identical in computation) exhibits octahedrally-coordinated alkali and transition metals, and is the lowest-energy phase at high sodiation; while at $x = 0.67$, a two-layer structure with prismatically coordinated Na ions (P2) is the ground state phase. Thus, though the DFT energy differences are small, thermodynamic considerations imply that P2 should be the equilibrium phase for $Na_{0.67}CoO_2$ at low temperatures. However, the experimentally observed behavior is different. Figure 1b summarizes the *ex situ* experimental synthesis results for the different Na_xCoO_2 polytypes [26]. At low Na content ($0.6 < x < 0.75$), P2 is only synthesized above 1000 K, while P3 and O3' are obtained at lower temperatures. Thus, the metastable phase three-layer polytypes are the actually observed low-temperature phases, while the two-layer P2 phase can only be synthesized at high temperature, in apparent contradiction with the DFT stability predictions.
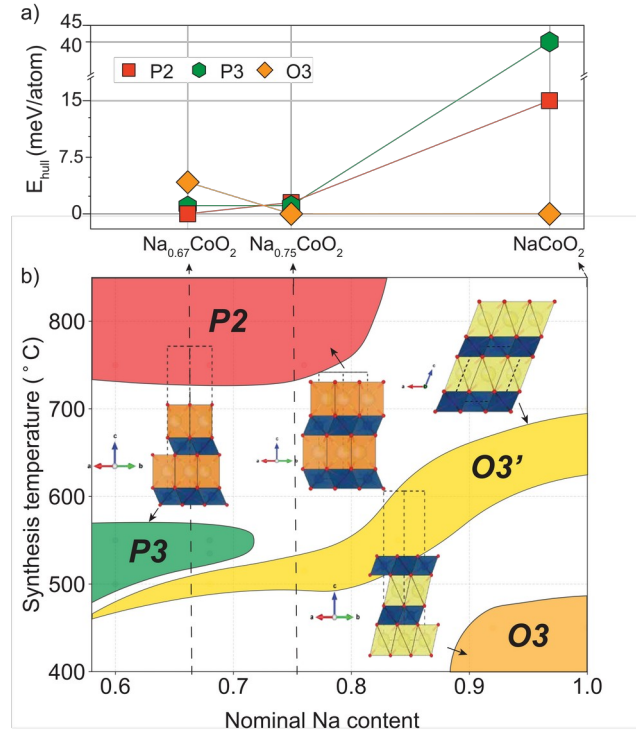
5

Figure 1: a) Energy above the convex hull (E_{hull}) of the various polytypes of Na_xCoO_2 in their lowest energy Na/vacancy configuration at x = 0.67, 0.75 and 1, calculated with the DFT-SCAN metaGGA functional [27]. b) Sodium layered oxides Na_xCoO_2 experimentally stabilized as a function of their sodium content x and of the temperature at which they are commonly synthesized in air. Areas denoted by P2, P3, O3' and O3 in different colors are single phase regions suggested by Lei et al.[26], representing the literature prior to this work. The crystal structure of each polymorph is shown and labeled using the notation introduced by Delmas [20]: the letter stands for the type of Na environment (P: prismatic, O: octahedral), while the number describes the oxygen stacking (e.g. in P2 Na ions occupy prismatic sites in between ABBA oxygen stacking). Blue units represent CoO_6 octahedral environments, yellow/orange units NaO_6 octahedral/prismatic environments. A prime symbol (e.g. P3') indicates a monoclinic or orthorhombic distortion (note that P3' is a monoclinic low-temperature distortion of P3. A P3 - P3' reversible transition occurs at 350-370 K [28]). Note that the crystallographically-distinct O3/O3' and P3/P3' phases are not distinguished computationally due to the relaxation of symmetry constraints.

Driven by the need to understand what drives solid-state reactions in polytypic Na_xMO_2 systems, we undertake an in-depth study of the synthesis of Na_xCoO_2 and Na_xMnO_2. Using *in situ* synchrotron X-Ray diffraction and differential scanning calorimetry (DSC), we observe a sequence of non-equilibrium three-layer phases during the solid-state ceramic synthesis of P2 layered sodium metal oxides. We rationalize our findings using an *ab-initio* thermodynamic framework based on a powder precursor interfacial reaction model, and suggest a unifying principle that governs the initial phase formation in solid-state synthesis. Our work elucidates the subtle competition between thermodynamics and kinetics, providing fundamental insights towards a more rational understanding of solid-state ceramic materials synthesis.

Results

***In situ* experimental study of P2 Na_xCoO_2 synthesis**

High-energy synchrotron X-ray diffraction (XRD) is a powerful tool to monitor the structural changes and phase evolution during inorganic materials synthesis [11, 12, 13, 14, 15]. To understand the formation of P2-Na_xCoO_2, we use *in situ* synchrotron XRD, observing the evolution of different phases from the

7

mixture of precursors to the final compound. We perform a set of *in situ* synthesis experiments, varying precursors, heating rate and annealing temperature, as described in the Methods and Supplementary Information (SI). CoO and Na_2O_2 are used as initial precursors, while Co_3O_4 and Na_2CO_3 are introduced later (see Figure S1 for a discussion on $Co(OH)_2$).

Figure 2 shows the result of a typical synthesis experiment: the formation of $Na_{\approx0.7}CoO_2$ from a ball-milled mixture of CoO + 0.35 Na_2O_2, with a fast heating rate (36 ℃/min) up to 850 ℃ in air. Only CoO is observed in the initial XRD scan, as Na_2O_2 amorphizes during ball-milling. The O3 phase with composition $NaCoO_2$ forms rapidly at 637 K (364 °C), about 7 minutes after the beginning of the synthesis (which starts at $\approx$100 °C). Figure 2b shows that, despite having a precursor ratio designed to target a $Na_{0.7}CoO_2$ stoichiometry, nearly all of the Na reacts with Co in a 1:1 ratio, represented by the reaction:
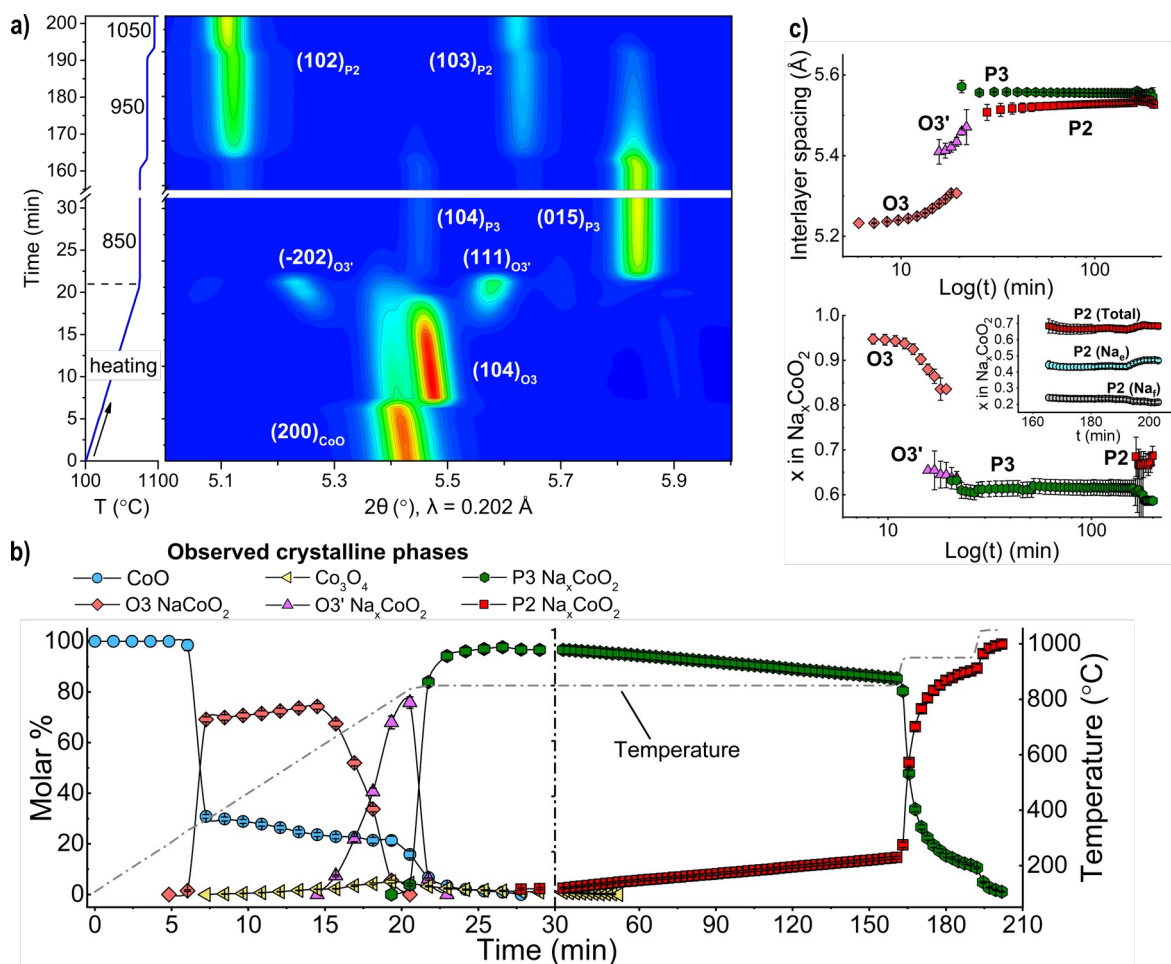
$CoO + 0.35\ Na_2O_2 = 0.7\ NaCoO_2 + 0.3\ CoO$

8
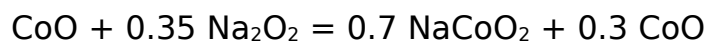
Figure 2: a) Solid-state synthesis of P2 $Na_{0.7}CoO_2$ monitored by in situ synchrotron XRD. The contour plot highlights the evolution of the Bragg peaks. A sequence of layered compounds is observed (O3 → O3' → P3 → P2). b) and c) Parameters obtained from Rietveld refinement of the XRD patterns. b) Evolution of the molar % of the observed crystalline phases and c) interlayer spacing and Na content of each Na_xCoO_2 polytype.

The reaction is extremely fast – it is complete in 1 scan (≈75 s) – and yields a crystalline O3-NaCoO₂ at nearly full sodiation (x = 0.95(1)). The rapid phase formation suggests a very fast oxygen uptake and diffusion of Na cations into the rock salt-type CoO framework, supported by rapid reorganization of the Co cations into layers [29]. Over the next fifteen minutes (T = 665 ˚C, ≈940

9

K), the evolution of interlayer spacing and Na occupancy show that the Na fraction in O3-Na_xCoO_2 decreases from 0.95 to approximately 0.8 (Figure 2c), after which a new monoclinic O3' phase with $Na_{0.65(3)}CoO_2$ composition appears. This change in Na_xCoO_2 stoichiometry results from a reaction between the residual CoO precursor with O3-$NaCoO_2$, as the system evolves towards the target composition. The O3 → O3' transition takes ≈6 minutes, after which O3' undergoes a rapid transition (< 75 s) to a P3 phase with large interlayer spacing (5.55 Å) and low Na content (0.61(2)). We speculate that the low Na content in the P3 phase indicates that some sodium may segregate from the layered oxide during the O3' → P3 phase transformation, likely as Na_2O. As P3 forms, the amount of CoO decreases rapidly, indicating that it reacts quickly with the O3' phase. Interestingly, this O3-O3'-P3 phase transformation sequence observed upon heating is similar to the phase evolution when an O3 oxide is desodiated electrochemically.[30]

Finally, when the temperature is maintained constant at 850 °C (≈1123 K), P3 transforms into P2- $Na_{0.67(2)}CoO_2$. Even though this is the highest temperature, the transition is the slowest: only 14.5(5)% of P2 has formed after 160 minutes. For this reason, we increased T to 950 °C and then 1050 °C, and finally obtained a single-phase P2 compound. As evidenced also by its smaller interlayer spacing, P2 accommodates a larger sodium content than P3, confirming that the Na formerly segregated was still available in the mixture.

10

In the SI we report complementary *in situ* experiments, showing that annealing at 550 ℃ results in a similar series of transformations, but without the formation of P2 (Figure S2). Moreover, the heating rate or choice of Co_3O_4 as precursor does not significantly influence the results of the experiment (Figure S2 to S5), proving that in the Na_xCoO_2 system this pathway is robust to synthesis variations. We show later that this is not the case when a Na_2CO_3 precursor is used.

a)

exothermic ↑
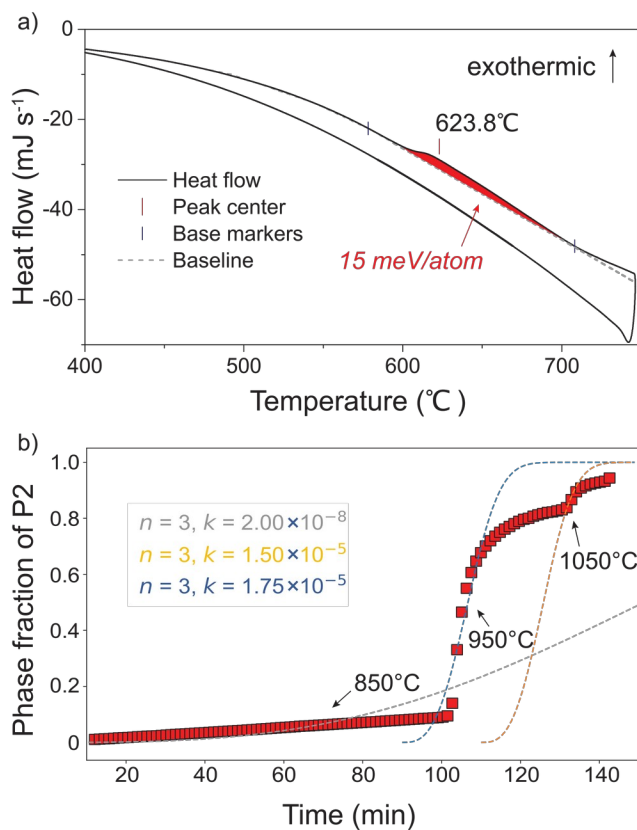
623.8℃

Heat flow
| Peak center
| Base markers
---- Baseline

15 meV/atom

Heat flow (mJ s^{-1})

Temperature (℃)

b)

$n = 3, k = 2.00×10^{-8}$
$n = 3, k = 1.50×10^{-5}$
$n = 3, k = 1.75×10^{-5}$

1050°C

950°C

850°C

Phase fraction of P2

Time (min)

Figure 3: a) DSC curve of pure P3'-Na$_{0.67}$CoO$_2$ powder (12.67 mg). An exothermic peak is observed at ≈624 ℃. The amount of heat released in this phase transition is calculated by integrating the shaded area. b) Phase fraction vs. time during the P3 to P2 transition obtained from Rietveld refinement and the corresponding fitting by the Avrami equation for 3 temperature ranges (850℃, 950℃ and 1050℃) independently. Note that P3 (Na$_{0.61}$CoO$_2$) to P2 (Na$_{0.67}$CoO$_2$) is not a constant-composition phase transition: it is limited not only by reaction kinetics but also by Na diffusion, which can explain the deviation from perfect Avrami fitting near the end of the transition.

According to the DFT stability calculations of Na$_x$CoO$_2$ in Figure 1a, P2-Na$_{0.66}$CoO$_2$ is the equilibrium phase at low temperature. To confirm that the observed P3 to P2 transition is indeed an irreversible transformation from a metastable to a stable phase, as opposed to a reversible temperature-driven first-order phase transition, we performed differential scanning calorimetry on a sample of P3'-Na$_{0.67}$CoO$_2$. Figure 3a shows that upon heating, an exothermic peak is observed at ≈624 ℃ and no transition is present upon cooling. After the measurement, we verified by XRD that the P3' sample had become P2, meaning P2 is indeed lower in energy than P3', confirming the DFT stability calculations. Furthermore, we confirm that P2 obtained from P3' via annealing at 750 ℃ never reverts back to the initial P3' structure upon annealing for long times at lower temperatures (Figure S6). Finally, the phase fraction evolution during the P3-P2 transition follows a characteristic S-shaped profile for which the transformation rate is low at both the beginning and the end, but rapid in the middle of the reaction. This profile

12

can be explained and fit by a nucleation-growth-saturation model which is qualitatively expressed by an Avrami equation (Figure 3b) [31]. The Avrami-like behavior together with our DSC result confirms that P3 → P2 is an exothermic, irreversible phase transformation driven by crystallization kinetics.

Rationalizing the phase evolution of Na$_x$CoO$_2$

The observed multistage phase evolution in Figure 2 can be classified into two major reaction sequences. First, there are a series of fast transformations that occur within 30 minutes, which proceed through the non-equilibrium three-layer phases O3-O3'-P3, with decreasing Na concentration from O3-Na$_{0.95}$CoO$_2$ to P3-Na$_{0.61}$CoO$_2$. Second, we observe a slow polymorphic transformation from the metastable P3 phase to the target equilibrium P2 polytype, which proceeds over the next 150 minutes.
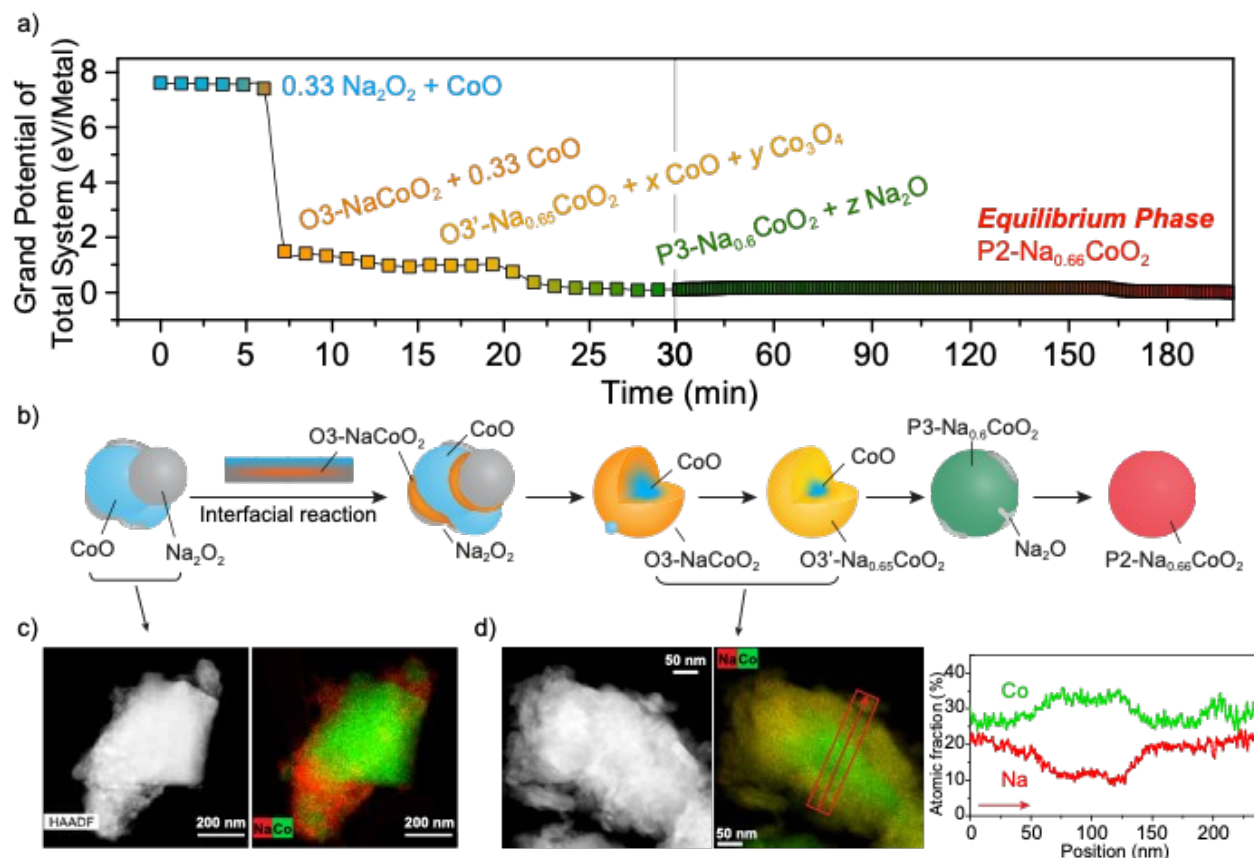
13

Figure 4: a) Evolution of the grand potential open to an external oxygen reservoir of the total system in the reaction vessel normalized by the number of metal cations (Na, Co). Two different scales are used in the time axis to highlight the multiple phase transitions in the first 30 minutes (same as figure 2b). b) Cartoon suggesting a physical model of the reaction pathway via interfacial reactions. c),d) High-angle annular dark-field scanning transmission electron microscopy (HAADF-STEM) and energy-dispersive X-ray (EDX) images showing the pristine $CoO+0.35Na_2O_2$ powders mixture (c), and the same mixture recovered after a brief annealing at 400 °C for 90 minutes (d). The STEM-HAADF and EDX images show an imperfect core-shell reaction, with sodiation proceeding inwards from the cobalt oxide particles surface.

To understand the thermodynamic evolution of the system, we plot the grand canonical free energy of the entire reaction vessel as a function of

14

time, shown in Figure 4, accounting for open boundary conditions with respect to oxygen as controlled by its chemical potential μ_{O_2}(Methods). The energy cascade shows that nearly all of the reaction free energy is consumed within the first 30 minutes of the solid-state reaction. Notably, ≈85% of the available reaction energy is consumed 6 minutes into the reaction to form $O3$-$NaCoO_2$. The transformations from O3 to O3' and then P3 consume much of the remaining reaction energy, leaving < 2% of the total reaction energy for the polymorphic transformation from P3 to P2.

Our energy cascade rationalizes the observed reaction sequence. The fast transformations that occur in the first 30 minutes are *thermodynamically*-driven by large reaction driving forces. The highest energy reaction is in the formation of $O3$-$NaCoO_2$, which then transforms to the non-equilibrium O3' and P3 phases. It is well-known that displacive transformations are facile between the three-layer polytypes; O3' is a monoclinic distortion of $O3$-$NaCoO_2$ associated with Na removal, and P3 can be formed from O3 by sliding the oxygen layer across the Na layer by (1/3, 1/3, 0) [17, 26, 32]. On the other hand, deriving the P2 phase from O3 requires sliding of the oxygen layer across the Co layer, which has too large an energy barrier to occur by a diffusionless transformation (Figure S7 and S8), likely proceeding by P2-nucleation instead. However, after 30 minutes, there is so little thermodynamic driving force remaining that higher temperatures are needed

15

to accelerate the Avrami (JMAK) kinetics of the P3→P2 polymorphic transformation.

Despite preparing a Na:Co precursor ratio to target the $Na_{0.7}CoO_2$ composition, the first phase to form is $O3$-$NaCoO_2$. The early formation of this three-layer intermediate consumes a significant fraction of the reaction energy, and it seems to determine the reaction path by setting the system up for the kinetically-facile topotactic transformations through the metastable O3' and P3 three-layer phases. Thus, rationalizing the initial formation of the O3 phase is crucial towards understanding the phase evolution in this system.

What is the mechanism driving this initial $O3$-$NaCoO_2$ phase selection? We can achieve some insight towards this question by considering that under slow diffusion conditions, as is the case in solid-state ceramic synthesis, reactions between precursors initiate at the precursor powder interfaces (Figure 4b). While $Na_{0.7}CoO_2$ is the composition of the entire reaction vessel, powder precursors of Na_2O_2 and CoO locally at their interface have no knowledge of the total stoichiometric composition of the system. Under these local interfacial boundary conditions, the first nucleus to form has, in principle, a compositionally-unconstrained reservoir of Na and Co to form from, for a given applied μ_{O2}. We demonstrate here that the first phase to form at this interface is the phase, or set of phases, with the maximum

reaction energy from the precursors. The stoichiometry of this reaction product is compositionally-unconstrained; in other words, this maximum reaction energy compound could have any Na/Co ratio—regardless of the prepared precursor ratio. When oxygen transport is fast, the oxygen stoichiometry of the product will be set by the μ_{O2} of the reaction atmosphere.

The reaction energies to various Na_xCoO_2 phases in a reaction between CoO | Na_2O_2 precursors in air is shown in Figure 5, calculated from a thermodynamic grand potential open to an external oxygen reservoir [1, 33], using a methodology as described in Richards et al. [34]. The temperature-dependence of the free-energy is dominated by the entropy of gaseous O_2, and can be approximated without consideration of the entropy in the solids (Methods). Figure 5a shows that at all temperatures, the $NaCoO_2$ composition has the most negative reaction energy of all layered Na_xCoO_2 compositions at the $Na_2O_2|CoO$ interface, and is therefore the composition with the strongest driving force to form. The crucial observation is that *structure-selection* of the first-phase to form is largely governed by *composition-selection* of the maximum compositionally-unconstrained reaction energy. Specifically, the O3 polytype is the ground-state structure for the $NaCoO_2$ composition (Table S1, Figure 1 and S9), which itself has the highest negative reaction energy under open-system boundary conditions.
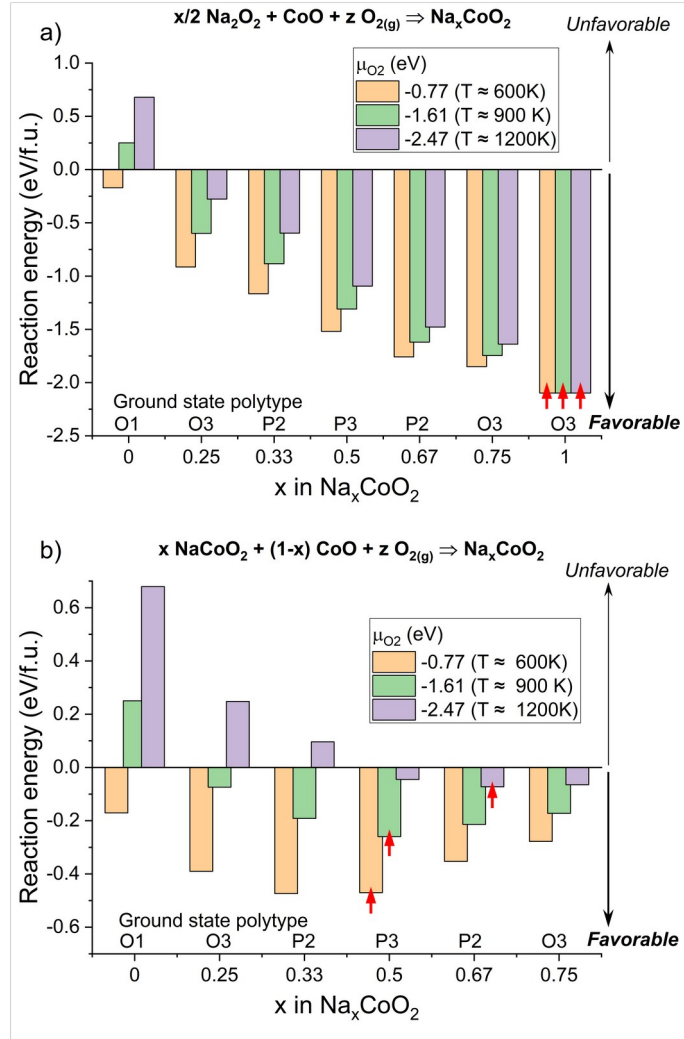
17

Figure 5: Reaction energies for the formation of the lowest-energy Na_xCoO_2 polytype as a function of x: (a) for the reaction (1) $x/2\ Na_2O_2 + CoO + z\ O_{2(g)} \rightarrow Na_xCoO_2$ and (b) for the reaction (2) $x\ NaCoO_2 + (1-x)\ CoO + z\ O_{2(g)} \rightarrow Na_xCoO_2$. $NaCoO_2$ and $Na_{0.75}CoO_2$ are O3-type structures, while $Na_{0.67}CoO_2$ is P2. The temperatures indicated in the legend correspond to $p_{O2} = 1$ atm, and are approximate (Methods). Red arrows indicate the most negative reaction energy bars, for each given μ_{O2}.

Since the precursors were prepared at a $Na_{0.67}CoO_2$ composition, the initial formation of O3-$NaCoO_2$ at $\approx$600 K leaves remaining CoO precursor in the reaction vessel (Figure 2b). The nucleation of P2-$Na_{0.67}CoO_2$ around 30 minutes can further be rationalized by computing the compositionally-unconstrained μ_{O_2}-dependent reaction energy between CoO and O3-$NaCoO_2$. As shown in Figure 5b, at high temperatures it is increasingly difficult to make layered oxides of low Na content, whereas at lower T they become favorable. At the CoO|O3-$NaCoO_2$ interface (Figure 5b), above 900 K the most favorable composition to form is $Na_{0.67}CoO_2$, for which the ground state structure is the P2 polytype (Table S1). Thus, there is a thermodynamic driving force towards nucleating the P2 compound during the multistage phase evolution. However, while the lowest energy structure at $Na_{0.67}CoO_2$ composition is P2, the computed P2/P3 energy difference is small (1 meV/atom) so that the reaction sequence O3→O3'→P3 and O3→O3'→P2 are both thermodynamically competitive. The fact that the P3 intermediate is observed experimentally is due to the kinetically-facile layer-shifting from O3'→P3, versus O3'→P2. Indeed, we find that O3' and P3 are already observed even below 550 °C (Figure S2 and Figure S3). Our results show that when thermodynamic driving forces are small, kinetically-viable structural transformations drive structure-selection along the phase transformation pathway. The nucleation of the P2 polytype also likely occurs at low T (near 27 minutes, Figure 2), providing the germ nuclei for the Avrami reaction in

19

the slow polymorphic transformation regime, but such nuclei can only grow at a measurable rate at high temperature.

We conduct similar reaction analyses starting from a Co_3O_4 precursor (Figure S4, S5 and S10), and arrive at similar conclusions: we experimentally observe an analogous phase formation sequence O3→O3'→P3→P2 when annealing at 850 °C, while at 550 °C the formation of P2 from P3 does not occur. The initial formation of O3 appears to be even faster when using Co_3O_4. Like in the CoO case, our calculations illustrate that such initial O3 formation is driven by the fact that it has the most negative formation energy (Figure S10a). Then, at the Co_3O_4|O3-$NaCoO_2$ interface (Figure S10b), low temperatures close to 600 K are needed to reach the $Na_{0.67}CoO_2$ composition.

Validation in the Na_xMnO_2 system and effect of precursors

To validate our hypothesis that the first phase to form at powder precursor interfaces is the compound with the maximum compositionally-unconstrained reaction energy, we next conduct analogous *in situ* experiments in the Na_xMnO_2 system with varying sodium precursors, including Na_2CO_3. This has particular relevance considering that different synthesis outcomes are obtained when using Na_2CO_3 *vs.* Na_2O_2 is several

20

systems including α-NaFeO$_2$ [35] and NaNi$_x$Mn$_{1-x}$O$_2$ [36]. Figure 6 shows the observed phase evolution and reaction energetics for Na$_x$MnO$_2$ using Mn$_2$O$_3$ and either Na$_2$O$_2$ (Figure 6a - c) or Na$_2$CO$_3$ (Figure 6d - e). When Na$_2$O$_2$ is used, the fully sodiated phase O3'-NaMnO$_2$ is observed first (Figure 6a), before it quickly transforms into a Na-deficient P3 phase, similar to the phase evolution in the Na$_x$CoO$_2$ system. Figure 6b shows that the initial O3'-NaMnO$_2$ phase has the maximum reaction energy in the Na$_2$O$_2$|Mn$_2$O$_3$ compositionally-unconstrained reaction, consistent with the principle we derived from the Co system.

The subsequent nucleation of P3-Na$_{0.42(1)}$MnO$_2$, finally transforming into P2, can also be explained by the reaction model between NaMnO$_2$ and excess Mn$_2$O$_3$, as shown in Figure 6c. The final P2 is a pure hexagonal phase at 1050 °C, while after cooling it yields a mixture of hexagonal P2 (with Mn vacancies) and distorted orthorhombic P2´ (Figure S11), in agreement with the literature [37, 38]. Interestingly, after the formation of P3, O3' forms again and coexists with P2 (Figure S12). This behavior is the result of the influence of μ_{O2} on the O3'-P3 equilibrium, and can be well explained by our reaction energy calculation (Figure S13 and supplementary notes). In short, initially μ_{O2} is high (low T) and P3 is the favorable product. When T increases sufficiently (low μ_{O2}) the situation is reversed and O3' may form again. This can only occur if a sufficient amount of Na is available, which is the case for

Na$_x$MnO$_2$ because the formed P3 phase is found to have a lower Na content
(x = 0.42) than P3 in the Co phase (Figure S14).

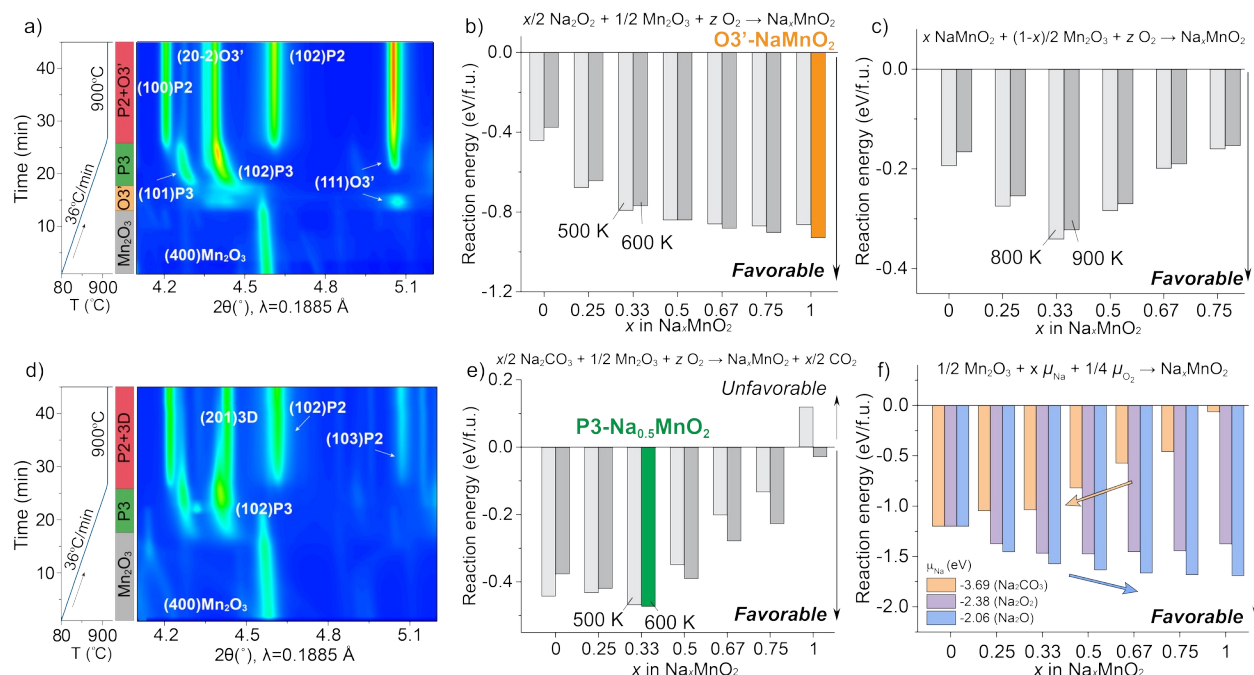Figure 6: a) In situ XRD pattern of the reaction between 1/2 Mn$_2$O$_3$ +1/3 Na$_2$O$_2$. Note that fully sodiated NaMnO$_2$ has a monoclinic distortion because of Jahn-Teller active Mn^{3+}, thus it is indicated as O3'. b) Reaction energies between Mn$_2$O$_3$ and Na$_2$O$_2$, according to the reaction x/2 Na$_2$O$_2$ + 1/2 Mn$_2$O$_3$ + z O$_{2(g)}$→ Na$_x$MnO$_2$. O3'-NaMnO$_2$ has the most negative formation energy at the beginning of the synthesis (≈600 K, orange bar). c) Reaction energies between Mn$_2$O$_3$ and O3'-NaMnO$_2$, according to the reaction x NaMnO$_2$ + (1-x)/2 Mn$_2$O$_3$ + z O$_{2(g)}$→ Na$_x$MnO$_2$ d) In situ XRD pattern of the reaction between 1/2 Mn$_2$O$_3$+1/3 Na$_2$CO$_3$; e) Reaction energies between Mn$_2$O$_3$ and Na$_2$CO$_3$, according to the reaction x/2 Na$_2$CO$_3$ + 1/2 Mn$_2$O$_3$ + z O$_{2(g)}$ → Na$_x$MnO$_2$ + x/2 CO$_{2(g)}$. P3-Na$_{0.5}$MnO$_2$ has the most negative formation energy at the beginning of the synthesis (≈600 K, green bar). f) Reaction energies between Mn$_2$O$_3$ and various sodium precursors at fixed μ_{O_2}(0 eV) according to

$$\frac{1}{2}Mn_2O_3 + x\,\mu_{Na} + \frac{1}{4}\mu_{O_2} Na_x MnO_2.$$ *The temperatures in b), c) and e) are approximate (Methods).*

Figure 6d shows that Mn_2O_3 reacts differently with Na_2CO_3 than it does with Na_2O_2. Instead of initially forming O3'-NaMnO$_2$, the sodium deficient P3 phase (P3-Na$_{\approx0.4}$MnO$_2$) appears. As the temperature increases, P3 transforms into a mixture of P2 and a phase with a 3D tunnel structure (3D-Na$_{\approx0.4}$MnO$_2$) [39]. Figure 6e shows the reaction energies between Mn_2O_3 and Na_2CO_3. Unlike the case when Na_2O_2 is the precursor, the sodium deficient phase P3-Na$_{0.5}$MnO$_2$ now has the most negative formation energy at intermediate temperatures (for example T = 600 K), explaining the different phase evolution observed experimentally. Again, the first phase to form in the Na$_x$MnO$_2$ systems is the compound with the most negative compositionally-unconstrained reaction energy.

Finally, we further revisit the CoO system with a Na_2CO_3 precursor, performing the *in situ* synthesis reaction of CoO + 0.35 Na_2CO_3, reported in Figure S15. We find that Na_2CO_3 is poorly reactive at low temperature, thus CoO oxidizes fully to Co_3O_4, which can then sodiate at higher temperature. Interestingly, the first phase to form is not O3-NaCoO$_2$: a P3 polymorph forms first, followed by P2. This is consistent with the results we obtained for the Mn system above and with our calculations (Figure S16).

23

In conclusion, despite the short *in situ* reaction times (< 1 hour), we are able to capture the first phase to form, and we validate the theory that the compound with the most negative compositionally-unconstrained reaction energy governs the composition and structure of the first phase to form. Additionally, our theory can rationalize how changing precursors influences this first phase. Different Na precursors (Na_2O_2 *vs.* Na_2CO_3) exhibit different sodium chemical potentials, which in turn create a different dependence of the reaction free energy as function of x in Na_xMO_2. In Figure 6f, we show that the higher the Na chemical potential in the precursor, the more the reaction free energies will tilt favorably towards compounds with high Na content. For the precursors with 'loosely-bound' sodium with high μ_{Na} (Na_2O: -2.06 eV, Na_2O_2: -2.379 eV), a fully sodiated O3 phase has the most negative formation energy, while as Na is 'locked up' in the stable Na_2CO_3 phase ($\mu_{Na}=¿$ -3.69 eV), the trend is reversed, resulting in the preferable formation of sodium deficient phases.

Discussion and Outlook

Understanding the role of thermodynamics versus kinetics during materials formation is a foundational question in materials processing and synthesis

24

science. Although qualitative heuristics for navigating these concepts are commonplace, it has been difficult to establish a quantitatively rigorous understanding of the competition between thermodynamics and kinetics for real synthesis reactions. This has been due to two reasons: 1) reactions occur in a 'black box', meaning that the initial phase evolution often remains unknown. 2) the energies of these reactions are difficult to measure as a function of reaction progress.

In this work, we leveraged *in situ* synchrotron X-ray diffraction to characterize the early stages of phase evolution for Na_xCoO_2 and Na_xMnO_2 materials during solid-state ceramic synthesis. Despite the traditional intuition that solid-state reactions are slow, we observed a number of fast reactions that take place within minutes of initiating synthesis. By combining the observed reaction pathways with *ab-initio* thermodynamics, we were able to show that the first phase to form can consume a majority of the total reaction free energy. Furthermore, this first phase may also topotactically template the structural evolution through further non-equilibrium phases. To rationalize the structure-selection mechanism of the first phase to form, we proposed a model where the first phase to nucleate at the interface between solid-state powder precursors is the compound, or set of compounds, with the maximum compositionally-unconstrained reaction energy. This first phase to form has the *composition* with the most negative reaction free-energy, and its *structure* is governed by the ground-state crystal structure at

25

this composition. We note that this mechanism is particularly relevant in reactions where thermodynamic driving forces are large, such as these solid-state chemical reactions. In synthesis methods at lower temperatures and with smaller driving forces (on the order of k_BT), such as in hydrothermal synthesis, structure-selection may instead be driven by size-dependent thermodynamics and competitive nucleation kinetics [14, 40, 41, 42, 43].

The compositionally-unconstrained powder reaction model has two major consequences: 1) the first-phase to form does not necessarily have the composition corresponding to the summed precursor composition, and 2) the first phase to form can be engineered by varying the precursors, as demonstrated by switching from a Na_2O_2 to a Na_2CO_3 precursor in both Co and Mn systems. This rationalization of the first phase to form creates a valuable design handle by which reaction paths can be tailored to go through, or circumvent, specific metastable intermediates.

While we often separate thermodynamics and kinetics conceptually, our analysis here shows that they are intimately coupled during the early stages of materials formation. Fast reaction kinetics during multistage crystallization are a consequence of large thermodynamic driving forces, whereas small driving forces lead to slow kinetics, requiring high reaction temperatures for reactions to complete. Moreover, the first-phase to form can be largely rationalized from thermodynamic arguments, when analyzed under the

26

appropriate reaction boundary conditions. While thermodynamics seems to drive the initial composition selection, the ensuing transformations can often be kinetically-selected by simple composition variations, or by topotactically-facile layer shifting, as is the case in the layered compounds that we studied. By better understanding the intricate relationship between thermodynamics and kinetics during materials formation, this work facilitates the design of more sophisticated strategies towards the targeted synthesis of inorganic materials.

Methods

Synthesis and experimental characterization

O3 $NaCoO_2$ was synthesized using a conventional solid-state method. Stoichiometric amounts of Co_3O_4 (Aldrich, 99.5%, nanopowder) and Na_2O_2 (Aldrich, 97%) were mixed thoroughly by a Spex Mixer/Mill 8000M for 90min. The precursors were then pressed into pellets before annealing at 450℃ for 16h under flowing oxygen. P3' $Na_{0.67}CoO_2$ was prepared by chemically desodiating O3 $NaCoO_2$. Stoichiometric amounts of O3 $NaCoO_2$ and NO_2BF_4 (Aldrich, $\geq$ 95%) were added to acetonitrile (Aldrich, 99.8%, anhydrous) in an Argon-filled glove box. NO_2BF_4 dissolves while Na_xCoO_2 remains as a solid

phase. The solution was then stirred for 2 days before the resulting black powder was filtered and washed three times with acetonitrile. The sample was then dried at 70 ℃ in vacuum overnight and stored in the Argon-filled glovebox.

The differential scanning calorimetry (DSC) measurement were performed using a SDT Q600 system (TA Instruments). 12.67 mg of P3' $Na_{0.67}CoO_2$ powder was heated from room temperature to 750 ℃ at a heating rate of 5 ℃/min under flowing Argon, then cooled at the same rate. The powder after DSC was recovered and used for XRD analysis using a Rigaku diffractometer, in Bragg–Brentano geometry with Cu Kα radiation.

For the *in situ* synthesis, we target the formation of $Na_{0.7}CoO_2$ by using different oxide precursors (CoO (Alfa, 99.995%) and Co_3O_4) with Na_2O_2 as sodium source. Two sets of precursors were mixed (Spex Mixer/Mill 8000M for 90min), pelletized and then annealed at 550 and 850 ℃ in air, respectively. Two heating rates were used, one fast (36 ℃/min) and one slow (0.5 ℃/min). A synthesis experiment was also done using a mixture of CoO and Na_2CO_3. For the *in situ* synthesis of Na-Mn-O system, two sets of precursors, $0.67Na_2O_2+Mn_2O_3$ and $0.6Na_2CO_3+Mn_2O_3$ were mixed (Spex Mixer/Mill 8000M for 90min), pelletized and then annealed at 900 ℃ in air, respectively, with a heating rate of (36 ℃/min). *In situ* synchrotron X-ray diffraction was performed at F2 (CHESS) and 28-ID-2 (NSLS-II, BNL) for the

28

experiment in the main text. 28-ID-2 (NSLS-II, BNL), F2 (CHESS) and 17-BM-B (APS, ANL) were used for experiments in the Supp. Info. Each scan takes ≈12 seconds and the interval between the end of a scan and the beginning of the next one is one or three (varying from experiment to experiment) minutes (for data processing). The in situ synthesis experiment using Na_2CO_3 and CoO was performed in a Bruker D8 diffractometer using Bragg-Brentano geometry (starting from 200 °C, a 1 hour-long XRD scan is taken every 50 °C).

For TEM, the powder samples were diluted in hexane and sonicated to obtain good particle dispersion. The TEM samples were prepared by drop casting the solution onto a standard 400 copper mesh TEM grid with lacey carbon support. The samples were loaded into a Gatan 648 vacuum-transfer holder to transfer the sample from the glovebox to the microscope in an inert Ar atmosphere. The HAADF-STEM and EDX maps were performed on a FEI TitanX 60-300 microscope equipped with the Bruker windowless EDX detector at an acceleration voltage of 200 kV. The particles size for the Co and Mn oxides used in our experiments is found to be of a few hundred nanometers (100-400 nm) after ball-milling of the precursors mixture. Na precursors retain instead little crystallinity and have smaller particles size.

Rietveld refinement was carried out using Fullprof. Multiple phases were included in each refinement. A point-by-point background was manually

29

selected. Zero-shift value was refined in the first scan and then kept constant for all subsequent scans. Peak shapes were modeled with a Thompson-Cox-Hastings pseudo-Voigt function (Npr=7). U, V, W, X, Y values were kept constant as possible between scans, although the subsequent nucleation of different phases induced peak width variation and thus made it necessary to refine them (mostly X). Unit cell parameters were always refined for all phases. Fractional atomic coordinates, site occupancy factors and Debye-Waller factors, as a rule of thumb, were refined whenever the relative phase is more than $\approx$10 wt% to avoid divergence. Debye-Waller factors were refined as a common value for all atoms ($B_{overall}$) in a given phase. Refinements were deemed acceptable only when R_{bragg} of the main phases were consistently < 10.

First principles calculations

Spin-polarized density functional theory (DFT) calculations [44] were carried out using the Vienna Ab Initio Simulation Package (VASP) [45] and the projector-augmented wave (PAW) method [46]. Each calculation used a reciprocal space discretization of 25 $Å^{-1}$ and consisted of two sequential structural optimization steps, where both lattice parameters and atomic positions were relaxed in the absence of symmetry constraints. The threshold energy difference for self-consistent field (SCF) convergence in the total free energy was set to 1 x 10^{-3} eV, and a Gaussian-type smearing of the Fermi level was

applied. We note that the relative stability of various P2-Na$_x$CoO$_2$ configurations obtained using total energy convergence criteria of 1 x 10^{-3} and 1 x 10^{-5} eV yielded very similar results, so that the less stringent convergence criterion was deemed sufficient here. A plane wave energy cutoff of 520 eV was used throughout. The choice of the SCAN meta-GGA exchange-correlation functional was motivated by its accurate prediction of the energy and structure of materials with diverse bonding and its comparable efficiency to that of standard LDA and GGA functionals [27, 47, 48].

Construction of finite-temperature phase diagrams

To determine the energy above the convex hull of Na$_x$CoO$_2$ structures and construct a ternary Na-Co-O phase diagram, calculations were performed on O$_2$, CoO, Co$_3$O$_4$, Na$_2$O$_2$ and Na$_x$CoO$_2$ structures ($0 \leq x \leq 1$) using analogous parameters as those described above. The ground state Na/vacancy configurations of the various O3, P2 and P3 Na$_x$CoO$_2$ ($0 < x < 1$) phases considered in this work were determined in two steps. First, the energy of several hundred possible Na/vacancy orderings at different Na content was computed using the fast GGA+U functional. For all structures with energy below 50 meV/atom from the convex hull (between 60 and 300 Na/vacancy configurations, depending on the Na content) the ground state configuration was recalculated using the more accurate SCAN meta-GGA functional.

31

Finite temperature phase stability was evaluated by including the entropy of O_2 gas, while neglecting the entropy of all solid phases, as is common for equilibria against oxygen [1]. <mark>For a discussion of the role of entropy on the solid phases we refer the reader to the SI.</mark> The free energy of $O_2(g)$ is obtained as:

$$E_{O2} = H_{O2} - S_{O2} \times T, \qquad\qquad (1)$$

where H_{O2} is the 0 K formation enthalpy obtained for an isolated O_2 dimer using SCAN, and S_{O2} is the experimental entropy at the temperature (T) of interest obtained from the JANAF thermochemical tables [49]. Likewise, the free energy of $CO_{2(g)}$ was calculated as:

$$E_{CO2} = H_{CO2} - S_{CO2} \times T. \qquad\qquad (2)$$

Grand canonical reaction energy calculations

Reaction energies to form the ground state Na_xCoO_2 polytypes at various x contents were obtained from a grand-canonical ensemble description at different oxygen chemical potentials, μ_{O2}. As described by Ong et al.[1], μ_{O2} takes the form:

$$\mu_{O2}(T,p_{O2})=h_{O2}(T,p_0)-T\left(s_{O2}(T,p_0)-k\times\ln\left(\frac{p_{O2}}{p_0}\right)\right) \qquad (3),$$

where p_0 is the reference pressure, p_{O2} is the O_2 partial pressure and k is the Boltzmann constant. Lower case h_{O2} and s_{O2} denote the enthalpy and entropy of oxygen gas per O_2 molecule. In this work, μ_{O2} values are referenced such that $\mu_{O2}=0$ eV / O_2 under standard conditions of temperature and pressure (T = 298.15 K, and $p_{O2}=p_0=1$ atm). So while the trends we observe are meaningful, as proven in similar recent work [3], the exact temperature values may be offset with respect with experimental ones.

The relative chemical potential of Na in a particular Na precursor (for example Na_2O_2) in Figure 6f is defined as the difference between the precursor's formation energy and the chemical potential of all other elements in the precursor ($\dot{c}Na_2O_2:\mu_{Na}=\frac{1}{2}(\mu_{Na2O2}-\mu_{O2})$). For sodium binary oxides, the free energy of $O_{2(g)}$ at ambient temperature is taken as the reference μ_{O2}. For Na_2CO_3, the chemical potential of the $CO_{2(g)}$ at ambient temperature is taken as reference.

Constructing the Energy Cascade

The energy cascade is constructed by multiplying the *in situ* XRD observed phase fraction of each phase at a given time by its grand canonical free energy, $\Phi = G - n_O\mu_O$, using the μ_O value discussed above. The number of Na and Co ions are conserved throughout the entire reaction, while oxygen is in exchange with the open air reservoir, so the grand canonical free energy is normalized to the overall metal concentrations throughout the reaction; Na = 0.66, Co = 1. The Na_2O_2 phase is amorphous (XRD not well suited to its quantification), so we infer its phase fraction in the early stages of synthesis from the concentrations of CoO and $NaCoO_2$, where we assume that all the Na_2O_2 is consumed in this initial reaction. In the O3'$\rightarrow$P3 transformation, the Na concentration in the layered phase decreases from approximately 0.66 to 0.6. We assume the Na is ejected from the layer phase in an oxide form, whose grand free energy can be approximated by the energy of solid Na_2O. For the energy cascade, $\Phi = 0$ eV/metal is set to the grand free-energy of P2-$Na_{0.67}CoO_2$, which is the equilibrium phase at all temperatures throughout the reaction. Formation energies for intermediate *x* in O3-Na_xCoO_2 from 0.8 < x < 1.0 are derived from the ordered structures in Kaufman and Van der ven [50].

Acknowledgements

34

Bibliography

1. Ong SP, Wang L, Kang B, Ceder G. Li-Fe-P-O-2 phase diagram from first principles calculations. *Chemistry of Materials* 2008, **20**(5)**:** 1798-1807.

35

2.   Andersson JO, Helander T, Hoglund LH, Shi PF, Sundman B. THERMO-CALC & DICTRA, computational tools for materials science. *Calphad-Computer Coupling of Phase Diagrams and Thermochemistry* 2002, **26**(2)**:** 273-312.

3.   Bianchini M, Wang J, Clément R, Ceder G. A First-Principles and Experimental Investigation of Nickel Solubility into the P2 NaxCoO2 Sodium-Ion Cathode. *Advanced Energy Materials* 2018, **8**(26)**:** 1801446.

4.   Narayan A, Bhutani A, Rubeck S, Eckstein JN, Shoemaker DP, Wagner LK. Computational and experimental investigation for new transition metal selenides and sulfides: The importance of experimental verification for stability. *Physical Review B* 2016, **94**(4)**:** 045105.

5.   Sun WH, Dacek ST, Ong SP, Hautier G, Jain A, Richards WD*, et al.* The thermodynamic scale of inorganic crystalline metastability. *Sci Adv* 2016, **2**(11).

6.   Aykol M, Dwaraknath SS, Sun W, Persson KA. Thermodynamic limit for synthesis of metastable inorganic materials. *Sci Adv* 2018, **4**(4)**:** eaaq0148.

7.   Chen Y, Rangasamy E, dela Cruz CR, Liang C, An K. A study of suppressed formation of low-conductivity phases in doped Li7La3Zr2O12 garnets by in situ neutron diffraction. *Journal of Materials Chemistry A* 2015, **3**(45)**:** 22868-22876.

8.   Wang L, Bai J, Gao P, Wang X, Looney JP, Wang F. Structure Tracking Aided Design and Synthesis of Li3V2(PO4)3 Nanocrystals as High-Power Cathodes for Lithium Ion Batteries. *Chemistry of Materials* 2015, **27**(16)**:** 5712-5718.

9.   Eriksson R, Sobkowiak A, Ångström J, Sahlberg M, Gustafsson T, Edström K*, et al.* Formation of tavorite-type LiFeSO4F followed by in situ X-ray diffraction. *Journal of Power Sources* 2015, **298:** 363-368.

10.   Jensen KMØ, Tyrsted C, Bremholm M, Iversen BB. In Situ Studies of Solvothermal Synthesis of Energy Materials. *ChemSusChem* 2014, **7**(6)**:** 1594-1611.

11.   Shoemaker DP, Hu Y-J, Chung DY, Halder GJ, Chupas PJ, Soderholm L*, et al.* In situ studies of a platform for metastable inorganic crystal growth and materials discovery. *Proceedings of the National Academy of Sciences* 2014, **111**(30)**:** 10922-10927.

12. Jiang Z, Ramanathan A, Shoemaker DP. In situ identification of kinetic factors that expedite inorganic crystal formation and discovery. *Journal of Materials Chemistry C* 2017, **5**(23)**:** 5709-5717.

13. Martinolich AJ, Neilson JR. Toward reaction-by-design: achieving kinetic control of solid state chemistry with metathesis. *Chemistry of Materials* 2017, **29**(2)**:** 479-489.

14. Chen B-R, Sun W, Kitchaev DA, Mangum JS, Thampy V, Garten LM*, et al.* Understanding crystallization pathways leading to manganese oxide polymorph formation. *Nature communications* 2018, **9**(1)**:** 2553.

15. He H, Yee C-H, McNally DE, Simonson JW, Zellman S, Klemm M*, et al.* Combined computational and experimental investigation of the La2CuO4–xSx (0≤ x≤ 4) quaternary system. *Proceedings of the National Academy of Sciences* 2018, **115**(31)**:** 7890-7895.

16. Curtarolo S, Hart GLW, Nardelli MB, Mingo N, Sanvito S, Levy O. The high-throughput highway to computational materials design. *Nature Materials* 2013, **12:** 191.

17. Braconnier JJ, Delmas C, Fouassier C, Hagenmuller P. Electrochemical behavior of the phases Na_xCoO_2. *Materials Research Bulletin* 1980, **15**(12)**:** 1797-1804.

18. Lee M, Viciu L, Li L, Wang YY, Foo ML, Watauchi S*, et al.* Large enhancement of the thermopower in NaxCoO2 at high Na doping. *Nature Materials* 2006, **5**(7)**:** 537-540.

19. Takada K, Sakurai H, Takayama-Muromachi E, Izumi F, Dilanian RA, Sasaki T. Superconductivity in two-dimensional CoO2 layers. *Nature* 2003, **422**(6927)**:** 53-55.

20. Delmas C, Fouassier C, Hagenmuller P. Structural classification and properties of the layered oxides. *Physica B+C* 1980, **99**(1)**:** 81-85.

21. Delmas C, Fouassier C, Hagenmuller P. Relative Stability of Octahedral and Trigonal Prismatic Coordination in Layered Alkaline Oxides Axmo2 (X Less Than or Equal to 1). *Materials Research Bulletin* 1976, **11**(12)**:** 1483-1488.

22. Parant JP, Olazcuag R, Devalett M, Fouassie.C, Hagenmul.P. New Phases of Formula Na(X)Mno2 (X Less Than or Equal to 1). *Journal of Solid State Chemistry* 1971, **3**(1)**:** 1-+.

37

23. Yabuuchi N, Kubota K, Dahbi M, Komaba S. Research Development on Sodium-Ion Batteries. *Chemical Reviews* 2014, **114**(23)**:** 11636-11682.

24. Mo Y, Ong SP, Ceder G. Insights into Diffusion Mechanisms in P2 Layered Oxide Materials by First-Principles Calculations. *Chemistry of Materials* 2014, **26**(18)**:** 5208-5214.

25. Guo S, Sun Y, Yi J, Zhu K, Liu P, Zhu Y*, et al.* Understanding sodium-ion diffusion in layered P2 and P3 oxides via experiments and first-principles calculations: a bridge between crystal structure and electrochemical performance. *Npg Asia Mater* 2016, **8**(4)**:** e266.

26. Lei YC, Li X, Liu L, Ceder G. Synthesis and Stoichiometry of Different Layered Sodium Cobalt Oxides. *Chemistry of Materials* 2014, **26**(18)**:** 5288-5296.

27. Sun J, Ruzsinszky A, Perdew JP. Strongly Constrained and Appropriately Normed Semilocal Density Functional. *Physical Review Letters* 2015, **115**(3)**:** 036402.

28. Blangero M, Carlier D, Pollet M, Darriet J, Delmas C, Doumerc JP. High-temperature phase transition in the three-layered sodium cobaltite P ' 3-NaxCoO2 (x similar to 0.62). *Physical Review B* 2008, **77**(18).

29. Bianchini M, Fauth F, Hartmann P, Brezesinky T, Janek J. An in situ structural study on the synthesis and decomposition of LiNiO2. *Journal of materials Chemistry A* 2020**:** 10.1039/c1039ta12073d.

30. Delmas C, Braconnier J-J, Fouassier C, Hagenmuller P. Electrochemical intercalation of sodium in NaxCoO2 bronzes. *Solid State Ionics* 1981, **3:** 165-169.

31. Avrami M. Kinetics of Phase Change. I General Theory. *The Journal of Chemical Physics* 1939, **7**(12)**:** 1103-1112.

32. Delmas C, Braconnier JJ, Fouassier C, Hagenmuller P. Electrochemical Intercalation of Sodium in Naxcoo2 Bronzes. *Solid State Ionics* 1981, **3-4**(Aug)**:** 165-169.

33. Wang L, Maxisch T, Ceder G. A first-principles approach to studying the thermal stability of oxide cathode materials. *Chemistry of materials* 2007, **19**(3)**:** 543-552.

34. Richards WD, Miara LJ, Wang Y, Kim JC, Ceder G. Interface Stability in Solid-State Batteries. *Chem Mater* 2016, **28**(1)**:** 266-273.

35.   Takeda Y, Akagi J, Edagawa A, Inagaki M, Naka S. A Preparation and Polymorphic Relations of Sodium Iron-Oxide (Nafeo2). *Materials Research Bulletin* 1980, **15**(8)**:** 1167-1172.

36.   Fielden R, Obrovac MN. Investigation of the NaNixMn(1-x)O(2) (0 <= x <= 1) System for Na-Ion Battery Cathode Materials. *Journal of the Electrochemical Society* 2015, **162**(3)**:** A453-A459.

37.   Stoyanova R, Carlier D, Sendova-Vassileva M, Yoncheva M, Zhecheva E, Nihtianova D*, et al.* Stabilization of over-stoichiometric Mn4+ in layered Na2/3MnO2. *Journal of Solid State Chemistry* 2010, **183**(6)**:** 1372-1379.

38.   Kumakura S, Tahara Y, Kubota K, Chihara K, Komaba S. Sodium and Manganese Stoichiometry of P2-Type Na2/3MnO2. *Angew Chem Int Edit* 2016, **55**(41)**:** 12760-12763.

39.   Akimoto J, Hayakawa H, Kijima N, Awaka J, Funabiki F. Single-Crystal Synthesis and Structure Refinement of Na0.44MnO2. *Solid State Phenomena* 2011, **170:** 198-202.

40.   Sun W, Jayaraman S, Chen W, Persson KA, Ceder G. Nucleation of metastable aragonite CaCO$_3$ in seawater. *Proceedings of the National Academy of Sciences* 2015, **112**(11)**:** 3199-3204.

41.   Sun W, Kitchaev DA, Kramer D, Ceder G. Non-equilibrium crystallization pathways of manganese oxides in aqueous solution. *Nature Communications* 2019, **10**(1)**:** 573.

42.   Navrotsky A. Nanoscale Effects on Thermodynamics and Phase Equilibria in Oxide Systems. *ChemPhysChem* 2011, **12**(12)**:** 2207-2215.

43.   Ma X, Nolan AM, Zhang S, Bai J, Xu W, Wu L*, et al.* Guiding Synthesis of Polymorphs of Materials Using Nanometric Phase Diagrams. *Journal of the American Chemical Society* 2018, **140**(49)**:** 17290-17296.

44.   Hohenberg P, Kohn W. Inhomogeneous Electron Gas. *Physical Review* 1964, **136**(3B)**:** B864-B871.

45.   Kresse G, Furthmüller J. Efficiency of ab-initio total energy calculations for metals and semiconductors using a plane-wave basis set. *Computational Materials Science* 1996, **6**(1)**:** 15-50.

46.   Blöchl PE. Projector augmented-wave method. *Phys Rev B* 1994, **50**(24)**:** 17953-17979.

47. Kitchaev DA, Peng H, Liu Y, Sun J, Perdew JP, Ceder G. Energetics of ${\mathrm{MnO}}_{2}$ polymorphs in density functional theory. *Physical Review B* 2016, **93**(4)**:** 045132.

48. Yang JH, Kitchaev DA, Ceder G. Rationalizing accurate structure prediction in the meta-GGA SCAN functional. *Physical Review B* 2019, **100**(3)**:** 035132.

49. Linstrom PJ, Mallard WG. NIST Chemistry WebBook. *NIST Standard Reference Database Number 69*.

50. Kaufman JL, Van der Ven A. NaxCoO2 phase stability and hierarchical orderings in the O3/P3 structure family. *Physical Review Materials* 2019, **3**(1)**:** 015402.